

Receptogenesis in a Vascularized Robotic Embodiment

March 11, 2026

Kadri-Ann Pankratov*, Leonid Zinatullin, Hans Priks, Adele Metsniit, Urmas Johanson, Tarmo Tamm, Alvo Aabloo, Edoardo Sinibaldi*, Indrek Must*

K. A. P., L. Z., H. P., A. M., U. J., Prof. T. T., Prof. A. A., Assoc.Prof. I. M.
Institute of Technology, University of Tartu, Nooruse 1, 50411 Tartu, Estonia

E. S.

Italian Institute of Technology, Via Morego, 30, 16163 Genova, Italy

Email Addresses: kadri-ann.pankratov@ut.ee, edoardo.sinibaldi@iit.it, indrek.must@ut.ee

Keywords: *receptogenesis, polypyrrole, vascularization, open circulatory systems, vascular robotics, situated robotics*

Abstract

Equipping robotic systems with the capacity to generate *ex novo* hardware during operation extends control of physical adaptability. Unlike modular systems that rely on discrete component integration pre- or post-deployment, we envision the possibility that physical adaptation and development emerge from dynamic material restructuring to shape the body’s intrinsic functions. Drawing inspiration from circulatory systems that redistribute mass and function in biological organisms, we utilize fluidics to restructure the material interface, a capability currently unpaired in robotics. Here, we realize this synthetic growth capability through a vascularized robotic composite designed for programmable material synthesis, demonstrated via receptogenesis - the on-demand construction of sensors from internal fluid reserves based on environmental cues. By coordinating the fluidic transport of precursors with external localized UV irradiation, we drive an *in situ* photopolymerization that chemically reconstructs the vasculature from the inside out. This reaction converts precursors with photolabile initiator into a solid dispersion of UV-sensitive polypyrrole, establishing a sensing modality validated by a characteristic decrease in electrical impedance. The newly synthesized sensor closed a control loop to regulate wing flapping in a moth-inspired robotic demonstrator. This physical update increased the robot’s capability in real time. This work establishes a materials-based framework for constitutive evolution, enabling robots to physically grow the hardware needed to support emerging behaviors in a complex environment; for example, suggesting a pathway toward autonomous systems capable of generating specialized features, such as neurovascular systems in situated robotics.

1 Introduction

In unstructured environments, critical physical signals are not static features that can be precisely registered by a dedicated sensor, but rather emergent phenomena arising from the robot’s unique interactions with the environment [1]. This unpredictability exposes the insufficiency of static hardware, necessitating systems capable of constitutive evolution to physically instantiate the features needed to transduce these unique, situation-specific signals [2]. We need more focus on situated robots [3] that are deeply intertwined with its immediate surroundings and leverage the environment itself to guide its behaviour and expand its physical capabilities. Current robotics lacks morphogenetic mechanisms that couple environmental information with physical updates for expanding functionality.

In previous works, physical adaptability during deployment has been realised through compliance/deformation [4], configuration change (rearrangement) [5, 6, 7], growth [8], or software solutions[9]. Multi-substrate environments could be traversed by increasing locomotion plasticity with multi-purpose appendages that could be configured as thrusters, wheels, and legs [5]. Similarly, vastly different environments, such as aquatic and terrestrial, could be transversed with shape-morphing limbs [6] or body-wide morphological reconfiguration [7]. Remapping and fusing sensory feed according to situational awareness is a sign of robustness in current robots, e.g., by repurposing navigational accelerometers for gravimetry in the Curiosity rover [9]. A form of temporal adaptability is self-healing, e.g., recovering from damage by harnessing embedded polymer networks [10, 11]. As the next step, incorporating new material as the robot body can be achieved by including material from the environment, e.g., by combining soil and probe-deposited linker for root-inspired robots [8]. Functional body components such as grippers or sensing arrays could be retrofitted via physical additions (upgrades) on the robot body surface with advanced 3D printing [12]. In fluidic devices, tactile sensing could be retrofitted by measuring the single fluidic input [13]. All in all, current strategies to extend the robot’s capabilities during deployment rely on existing hardware or tailored retrofitting, with no new structurally and

functionally intertwined hardware generation.

When creating new hardware, the main bottleneck is the material - suitable material compositions should be placed at the optimal location. In nature, material transport in the organism is solved with passive mechanisms (diffusion) to reach molecule-level interactions (e.g., receptor binding) and active mechanisms (advection, particularly circulation) to minimize diffusion distance [14]. In robotics, the open circulatory systems of simpler organisms like arthropods serve as architectural models for designing material transport networks. They consist of a pumping element (heart), flow-directing arteries and hemolymph as a circulatory fluid that bathes the internal organs and infuses wings, as in Lepidoptera (Figure 1a). Insect wings are living structures [15], in which the hemolymph supports exoskeleton/cuticle hydration for stiffness modulation [16], thermal regulation [17], aerodynamic properties [16, 18] and chemical[19] and mechanical[20] signalling, providing an accessible (with effectively 2D fluid flow) case study for vascularised robotics.

Artificial interpretations of vascularisation are highlighted by progress in microfluidics, e.g, organ-on-a-chip or drug testing solutions [21], as well as structures for liquid transport [22]) and patterning [23]. In robotic systems, a multifunctional internal liquid was circulated throughout a lionfish-inspired robot, simultaneously powering and actuating it [24]. In terms of intra-fluid communication, Garrad *et al* demonstrated injecting patterned sequences of conducting and insulating fluid into a soft tube produces measurable resistance changes across embedded electrodes, encoding the fluidic input as a binary electrical signal [25]. In our previous work [26], we showed the integrative role of internal liquid for simultaneous body compliance modulation and muscle activation while reaching protovascular level, highlighting the capability of internal liquid to enable physically intelligent robotic systems. For living mammalian cells, oxygen diffusion distance is in the range of 100 μm to 200 μm [27] which gives clear motivation to develop vascular structures for cell viability in biohybrid systems [28] and hints to potential architectures for material-level *in-situ* morphogenesis. Robotic vasculature (a.k.a. embedded functional vias [29]) are proposed to alter robots' body properties in response to environmental conditions, offering a pathway to mimic phenotypic plasticity in organisms [29]. However, there are currently no reports on robotic vasculatures that close the loop from an environmental stimulus to a bodily adaptation, in part due to fabrication (printing) challenges.

Here, we report the *ex novo* generation of functional hardware components through an integrated vascular-materials strategy. To enable controlled matter transport, we introduce a vascularization approach that couples long-range advective flow with localized infusion. At the component level, we demonstrate that polypyrrole (PPy) synthesized via environmental UV-induced photopolymerization is a feasible UV-responsive receptor material. We validate our framework on a moth-inspired (Figure 1b, left) flapping-wing robotic platform (Figure 1b, right), where a circulatory fluid is routed through an engineered vascular network and used to deliver PPy precursors to the receptor site to be photopolymerized. This work advances autonomous robotic function in complex environments by extending morphological computation to the molecular scale, and provides a materials-centric and intrinsic dynamics driven perspective on neurovascular integration in robotic systems.

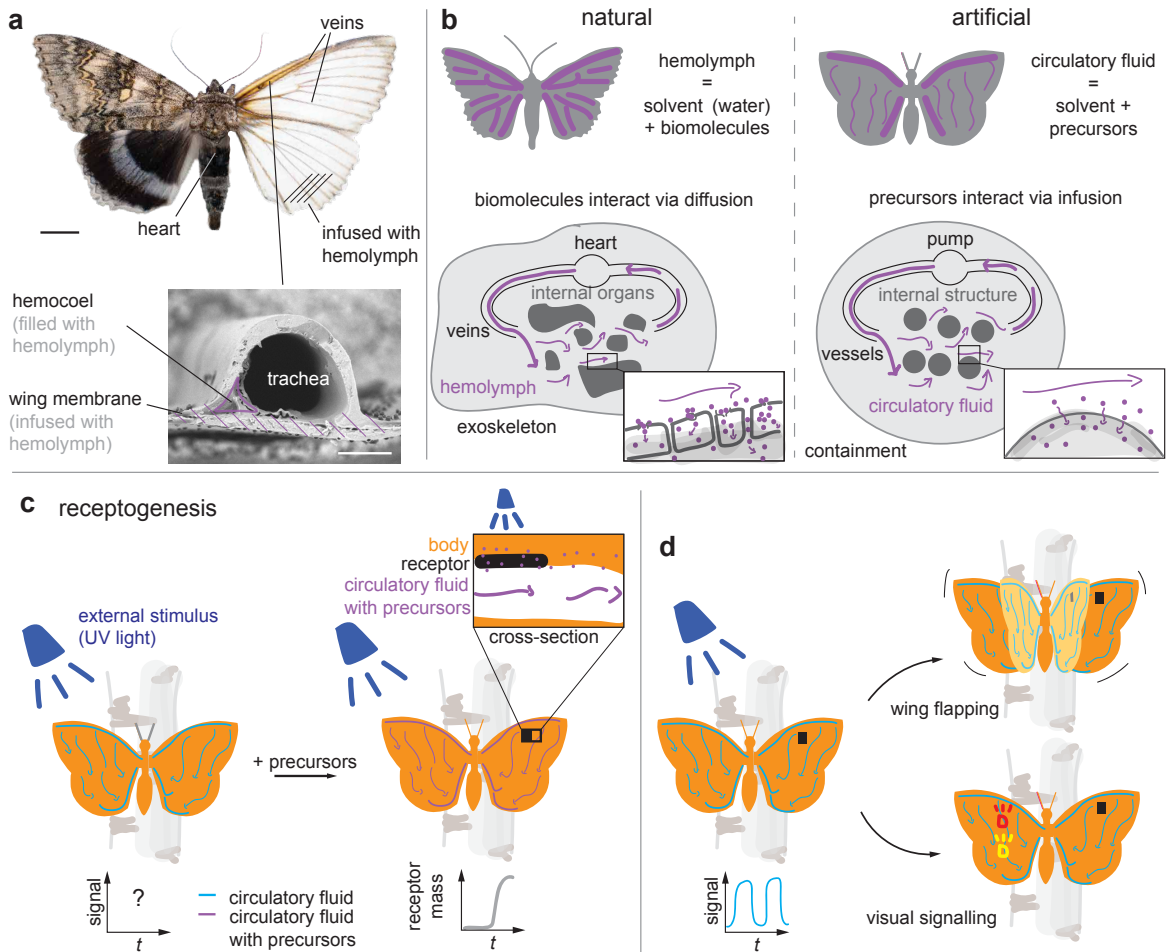


Figure 1: *Ex novo* hardware (receptor) generation in a moth-inspired vascular system: system concept
 a) Biological model. Dorsal view on *Catocala fraxini*, scales removed on the right wing to visualise wing veins. The SEM image inset shows a cross-section of a wing vein for carrying hemolymph. b) System components of a natural and artificial open circulatory system, respectively. Connectedness is achieved with directing fluid flow and interaction with internal elements. c) Receptorogenesis concept. Precursors introduced on demand to the vasculature form a receptive area in response to an externally applied stimulus. d) The local physical update gives access to receptor data (left) that closes emergent control loops, exemplified by regulating the flapping of artificial wings (top right) or visual signalling (bottom right). Scale bars (a) - 1 cm, (a, inset) - 100 μm

2 Results and Discussions

2.1 System Design

Figure 1c outlines the key steps of *ex novo* component generation using receptogenesis as a case study. We create functional components *in situ* by circulating precursors through an internal artificial vasculature and photopolymerising them with external stimulus (UV light). Inspired by the open circulatory systems of Lepidoptera (Figure 1b), we implement a 3D printed artificial vascular network that distributes material precursors throughout the body via global advection and local fluid infusion. We use polypyrrole (PPy) precursors for UV-sensitive receptor photopolymerization. This newly formed component functions as a light-responsive receptor capable of triggering downstream behaviours such as LED indication or wing flapping (Figure 1d). In our system, the stimulus that initiates receptogenesis and the signal being detected are incidentally the same, though the approach generalizes to a much broader class of stimuli and signals.

We chose polyethylene terephthalate glycol (PETG) as the 3D printing polymer as it is commercially available and transmits UV-light starting from 310 nm [30]. Pyrrole (Py) as an organic solvent infuses PETG and can be photopolymerised into PPy [31], during which the transparent Py forms dark UV-sensitive [32] PPy clusters. The perceived colour change is a convenient way of observing the synthesis process.

In our work, precursors are a liquid mix of pyrrole (acting as both monomer and solvent), a bis(4-methylphenyl)iodonium hexafluorophosphate initiator, and cellulose acetate propionate (CAP) as a structural modulator. We conceptualize this chemical inventory as a dual-source resource: it may be integrated as an on-board reservoir to ensure operational readiness, or alternatively, sequestered from the ambient environment via harvesting mechanisms. While the logistics of precursor procurement fall outside the primary scope of this study, the capacity for both intrinsic storage and extrinsic acquisition presents a robust framework for autonomous system evolution.

Surface-level modifications ("add-ons") often act as functional obstructions (analogous to intravascular clots) - limiting the functional versatility of the vascular system. Instead, we focus on the physical update (chemical synthesis) in the PETG matrix as opposed to the immediate vascular surface. In macroscale robots, however, diffusion alone is too slow to deliver precursor uniformly throughout the volume, limiting the rate at which the material can fully activate. To bypass this bottleneck, we implement advection that ensures rapid, uniform activation. We developed a global logistics network combining rapid fluid circulation through a vascular scaffold complemented by slower, diffusion-limited local precursors delivery via infusion into the PETG structure (Figure 2a). Fused deposition modelling (FDM) printing of PETG produced logistic highways (veins) by explicit definition and a distributed permeability structure (microchannels) by designed infill pattern (Figure 2b, Supplementary Figure S1). In the microchannels (Figure 2c), the circulatory fluid infused the volume of the PETG scaffold (Figure 2d), enabled by the large surface area in contact with the fluid. Pyrrole (Py) solution infused the PETG (exposure time approximately 20s) to an infusion depth of approximately 10 μm as seen from the element contrast in the SEM image in Figure 4d (bottom right). The formed Py-PETG layer was approximately 20% of the print line's thickness (50 μm radius). This enables us to achieve connectedness across multiple orders of scale (tens of centimeters via global transport and micrometers via infusion) using a single fabrication method.

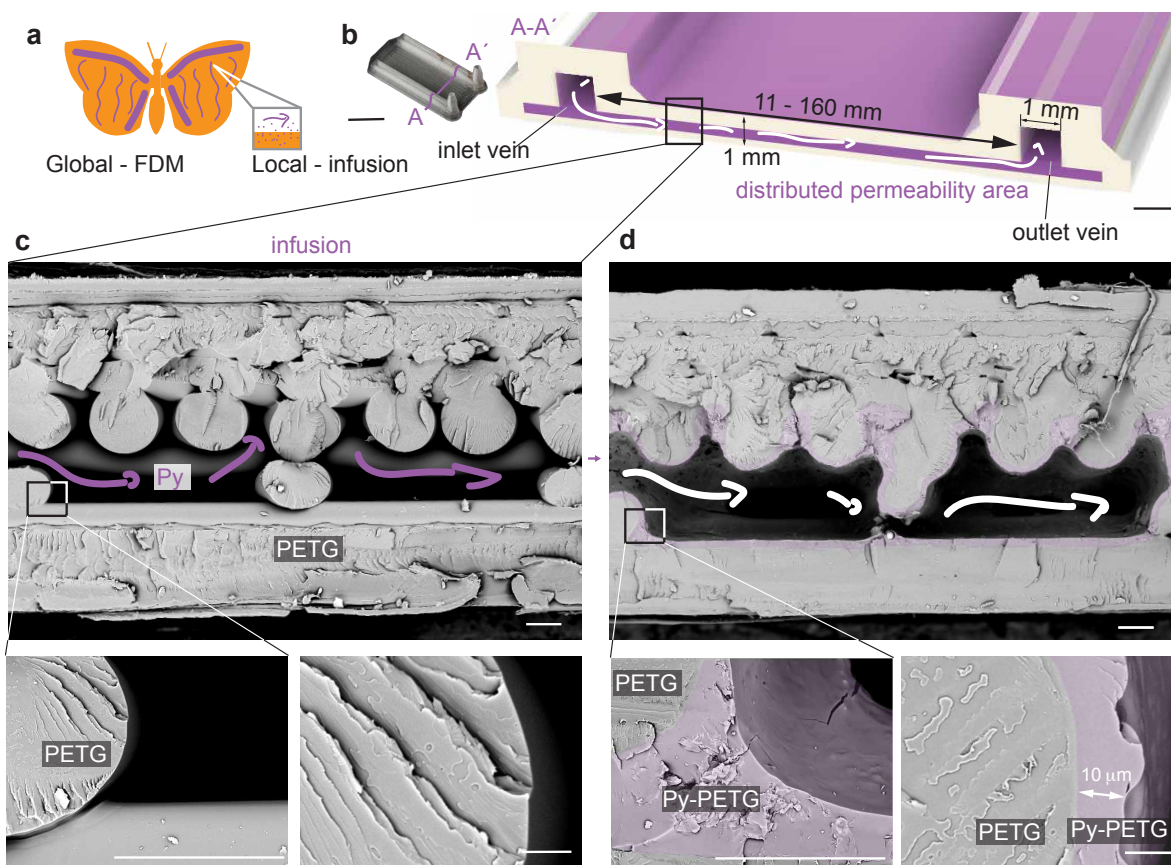


Figure 2: Multiscale vascularization. a) Vascularization hierarchies - global transport (FDM) and local interaction (infusion). b) Photograph and cross-sectional drawing of a global vascularised robotic composite consisting of veins and microchannels. c) SEM images of a non-infused structure, complementary space between the individual infill lines form a network of microchannels. d) SEM images of an infused (and thereafter dried) structure. Scale bars: (b, main) - 1 mm, (b, inset) - 10 mm, (c, d, main) - 100 μm , (c, d, insets) - 10 μm

2.2 Receptogenesis by In-vasculature Molecular Assembly

Receptogenesis is achieved via photopolymerization of Py precursors into a UV-receptive area induced by environmental UV-stimulus (Figure 3a). The circulatory fluid of precursors infuses the PETG structure (Figure 3b, Supplementary Movie 1) and forms an infused PETG (Py-PETG) region in the structure. Photopolymerization of Py is self-inhibiting as the synthesis takes place at the intersection of circulatory fluid infusion front and UV-light. Since PPy and the precursors absorb UV light, synthesis is preferentially localized at UV-exposed surfaces. Visually the synthesised area is dark colored. To characterise it, we monitored the 580 nm absorption *in-situ* during synthesis (Figure 3c). The absorption rate was -0.018s^{-1} and irreversible. We expect that the PPy formed clusters in the Py-PETG matrix that self-inhibit further growth when the immediate vicinity has been depleted of precursors as previously discussed in literature [31]. This is consistent with non-zero final transmittance of 580 nm in Figure 3c. Conduction combines electronic conduction of PPy clusters and electrolytic conduction of initiator in the PETG matrix surrounding the clusters, similarly to described elsewhere [33]. We demonstrated UV-PPy photolithography using a PETG negative contact mask (Figure 3d), achieving resolution 0.3 mm, limited by optical scattering by surface roughness.

PPy is sensitive to UV irradiation[34], which can photo-excite charge carriers and modify the population

or dynamics of polaron or bipolaron states (Figure 3e), leading to impedance decrease in our PPy-based system. The impedance change was registered by an embedded microprocessor unit featuring a custom bipolar pulse technique combined with voltage division by a constant external resistor (Figure 3f, left). The lower transient voltage across the receptive area (PPy-PETG), versus Py-PETG, showed higher conductance, whereas the lower voltage rate captured an increased capacitance (Figure 3f, right). Further, we encoded receptor response as a differential digital signal with LED readout, given the transient nature of polarons: the sensor response is characterized by its rate of change rather than absolute value. This parallels biological receptors, as we are not interested in absolute (impedance) values, but rather the change. As seen in Figure 3g, a drop in impedance corresponds to UV irradiation that was independently visualized with a red LED blinking.

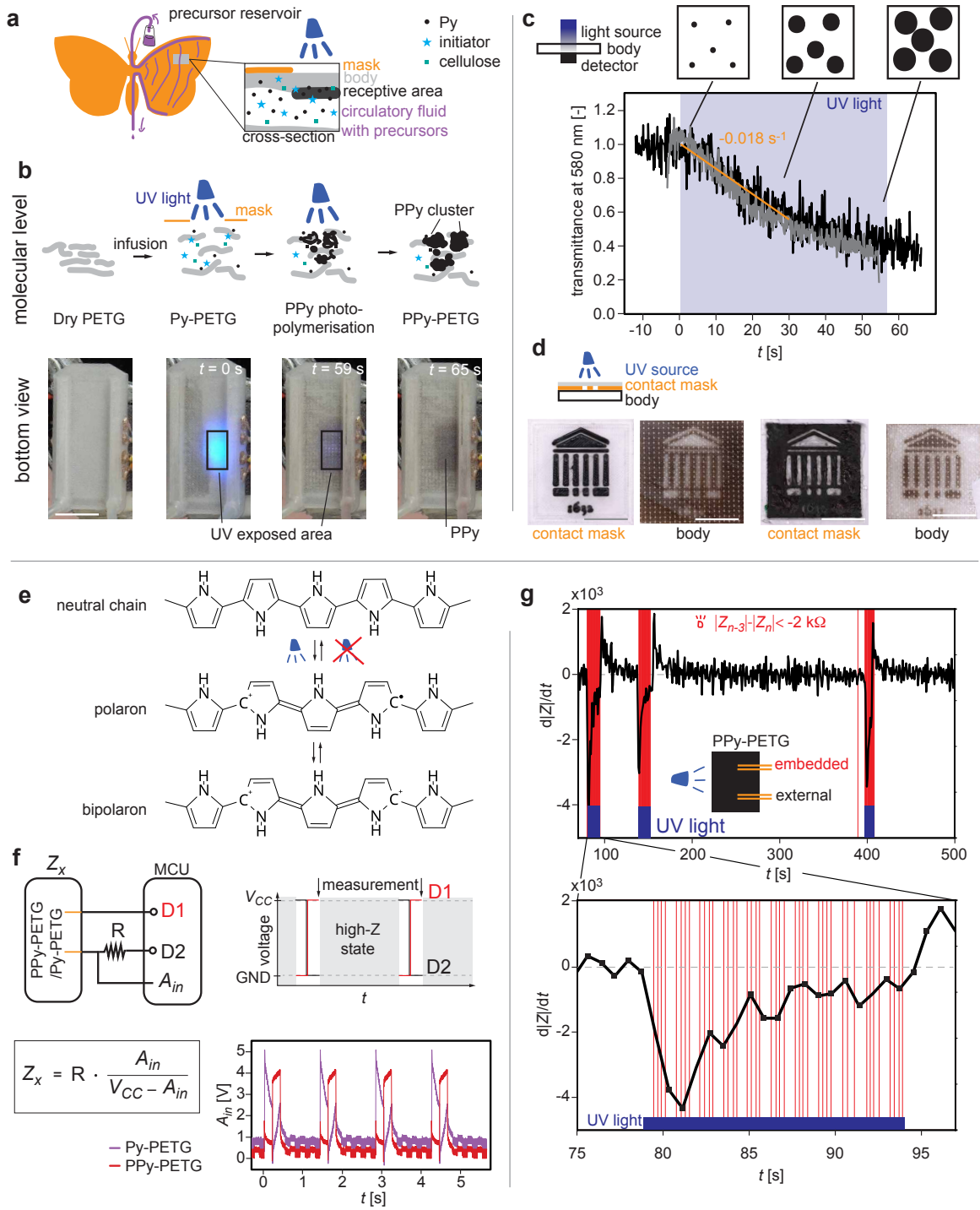


Figure 3: Receptogenesis based on PPy *in situ* photopolymerization a) The receptive area forms by local UV-exposure of the structure with precursors from the chemical inventory and distributed by a vascular system. b) Scheme of PETG infusion with precursors and in-situ photopolymerisation stimulated by an external UV light source (at 365 nm) (top). Transilluminative snapshots of photopolymerisation, where PPy synthesis is evidenced by the darkening (bottom). c) 580 nm transmittance through the receptive area decreases during photopolymerization, corresponding to nuclear growth of PPy clusters (insets). Black and grey lines correspond to two representative photopolymerization instances. d) UV-PPy photolithography demonstration on structure infused 7 days prior. e) UV induced temporary (bi)polaron: reaction scheme. Adapted from [35]. f) Embedded receptor: implementation using impedimetric readout (left) and demonstration (right). g) Impedimetric transient response (black) of receptive area to UV irradiation (blue) and modulated optical readout of the receptor (red). Scale bars: (b, d) - 1 cm

2.3 Robotic Demonstration

To demonstrate the efficacy of *ex novo* hardware fabrication for robots in environmental settings, we developed a representative moth-inspired platform (Fig. 4a). This demonstration highlights the synergy between environmental stimulus (UV-light) and body adaptation via material-level response (UV receptivity), which is expressed with behavioral outputs such as visual signalling and wing flapping (mediated by "central nervous system" represented by embedded microprocessors).

UV exposure permanently reduced the material's permeability and unlocked a latent UV-sensing capability, transforming it from a passive substrate into a functional receptive area through which the robot could transduce environmental cues into behavioral outputs. The robot started in minimal configuration, with embedded contacts representing latent positions of the receptors in PETG with nonexistent sensitivity to UV stimulus. The robot's operation represents co-expression of central strategic level and local material-level execution. Upon a central decision (suggesting the emergent need of UV receptivity in the future, not focused in this work), the robot casts a cocktail of precursors to the vascular system spanning the entire moth-shaped embodiment, vascular shadow area 175 cm², internal vascular volume of approximately 3 mL to prepare the embodiment for UV encounter. Internal circulatory fluid reached the entirety of the vascular structure, as seen in the timestamps of dry structure filled with isopropanol (Fig 4c, Supplementary Movie 2) and when adding blue tracer to the isopropanol (Fig 4d, Supplementary Movie 2). The liquid moves forward first in the leading vein and then to the directly connected distributed permeability area, pump advection assisted by wetting (capillary forces) and diffusion, respectively. Our system is resilient to many issues usually found when working with liquid in confined spaces (e.g. bubbles).

At low UV exposure (0.9 W LED at 20 mm), the prepared (Py-PETG, not PPy-PETG) embodiment did not sense UV (Supplementary Figure S2). Upon encounter of the prepared embodiment with intensive UV stimulus (1.6 W LED at 43 mm), the embodiment reacted by receptive area synthesis (Figure 4e, Supplementary Movie 3), which led to UV-responsiveness (sensitive to both 0.9 W test and 1.6 W synthesis LED) that completed the control loop by activating wing flapping or visual signalling without contribution by the central control level (Figure 4f, Supplementary Movie 4).

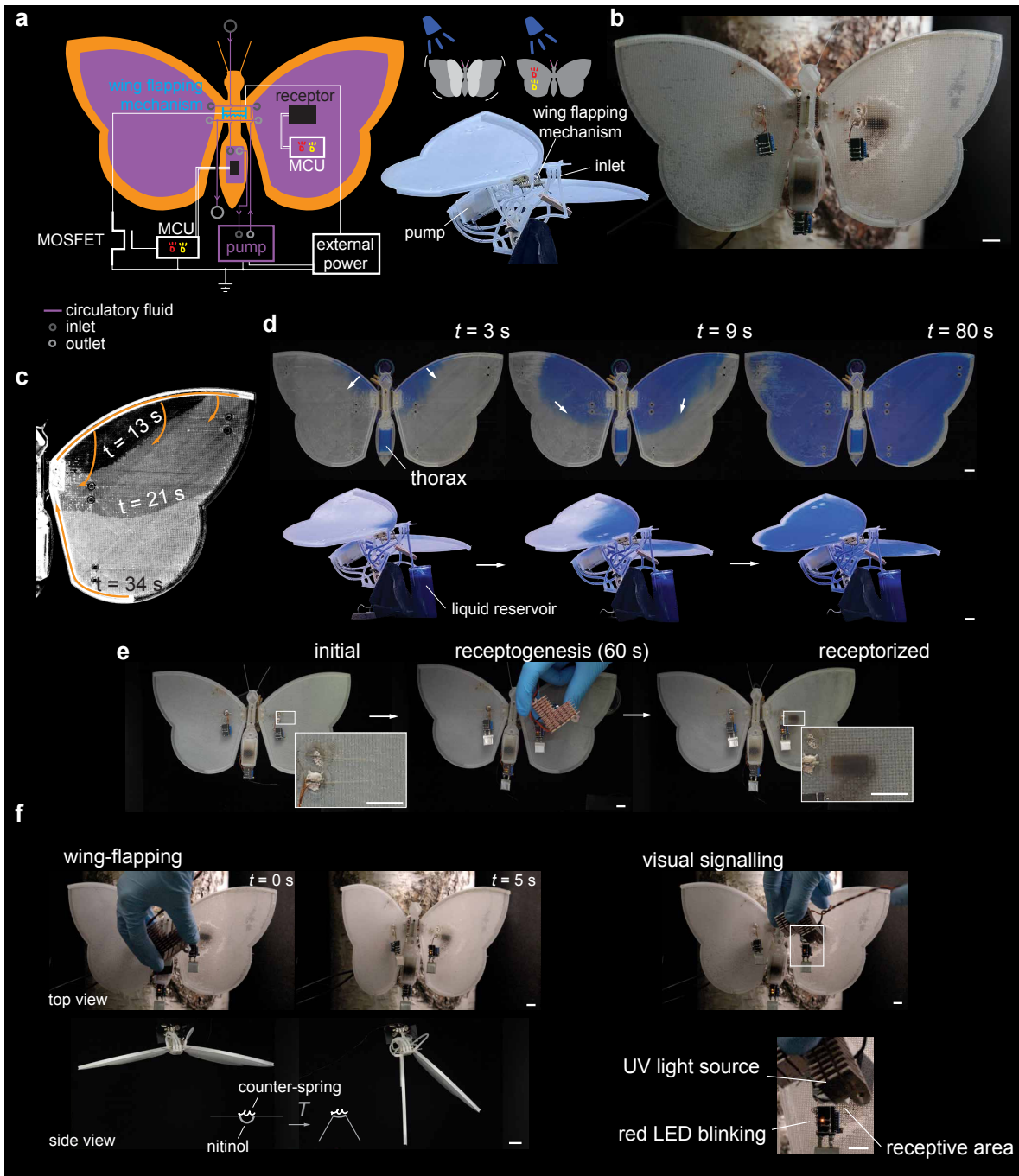


Figure 4: Illustrative robotic demonstration of *ex novo* hardware genesis. a, b) System implementation: a) scheme showing the fluid, control, and power lines and b) photograph. c, d) Illustrative filling of vascular system: c) air displaced with isopropanol (superimposed timestamps) and d) isopropanol displaced with isopropanol:water with blue tracer (sequential snapshots of top and isometric view) e) Wing-scale receptogenesis. f) The robotic moth reacts to UV-exposure to a receptive area in the thorax section by activation of the wing flapping mechanism and visual indication (LED flashing). Scale bars: 1 cm

2.4 Discussion

Chemistry is an undertapped toolkit in robotics that makes available a broader range of bodily modifications than reconfigurations of preassemblies, providing the desired match to real environments. The tight coupling between a chemical reaction and its environment — bridging molecular dynamics and macroscopic structure — provides the basis for natural intelligence as a kind of open-ended computation [36]. Chemical signals are used in multisensory neuromorphic computing [37], augmenting visual sensory data with olfactory context, similarly to biological organisms. Even when narrowly considering PPy, the case study material in this paper, the synthesis result is based on the precursor choice and environmental (synthesis) conditions, leading to wide range of possible outcomes (e.g., towards bioelectronic interfacing [38], ionic sensitivity [39], corrosion resistance [40], or electromagnetic wave shielding [41]). Even considering the light-patterning technique, external stimulus can modulate photocrosslinking patterns for microphase separation of a copolymer, achieving stiffness patterning in a chemically identical material [42], providing possible application scenarios in our vascularized system.

The realization of *ex novo* receptogenesis through vascularized material transport introduces a paradigm where physical adaptation is governed by molecular-scale interactions. In this framework, the computational burden for bodily modifications is offloaded to the interaction between environmental stimuli and molecular structures, where the synthesis process itself serves as the execution of a program that combines pre-determined bodily affordances (here, the PPy precursors) with situation-specific spatiotemporal information (here, local UV exposure). The newly synthesised hardware is a physical record of the environmental conditions. In the demonstrated case, the wing structure of the robotic lepidopteran transformed from a translucent, non-conductive state to a black, UV-sensitive "phenotype". This allows for the augmentation of existing robotic components through site-specific chemical changes, without digital symbolic representation, effectively bridging the groundedness gap between digital control and material reality.

The coordination of advection-based global transport and infusion-based local "last-mile delivery" caters to a high surface area and volume. At the subsystem level, the system enables high-density functionalization, suggesting a viable pathway towards organism/life-level intertwined hierarchical functionality that, within the current fabrication-centric paradigm, is challenging to fabricate and nearly impossible to modify or repair post-deployment. The high ratio between the total circulatory surface area and the footprint of individual components allows a centralized fluidic reserve to address and modify a vast number of discrete physical features, analogous to a single-wire architecture robustly managing complex electronic arrays. The vascular architecture retains compatibility with microfluidic precision manipulation and targeted delivery approaches; e.g., controlled wetting in the vasculature could target synthesis templated by a central command unit and executed in a distributed manner. Both levels of control - central and distributed - are needed in a practical system, but currently it is either one or the other, without vertical communication, which handicaps performance.

As shown in this study, vascularized composites devised to approach biological levels of adaptability pose challenges, e.g., with tailoring material compositions for suitable robotic preparedness. This challenge is increasingly supported by advancements in computational chemical programming [43] and machine learning [44], which allow for the design and testing of molecular structures and chemical reactions. By leveraging these computational tools, it is possible to design (multiple simultaneous) cascades for stimuli at the specificity similar to at the level of molecular receptors in biology. Materials capable of robot-wide physical actions establish a robust framework for constitutional evolution and the generation of *ad hoc* hardware in unstructured environments.

3 Conclusion

In conclusion, we demonstrated the *ex novo* generation (Figure 1) of UV-sensing hardware via photopolymerization within a moth-inspired, vascularized robotic embodiment. By employing a hierarchical vascularization strategy (Figure 2) - combining global advection defined by 3D printed structure with local infusion - we successfully distributed precursors (namely, pyrrole) across the body, enabling effective volume activation upon local exposure to environmental stimulus (UV-light). The resulting receptive area (PPy) exhibited a quantifiable impedance shift due to reversible (bi)polaron formation upon UV exposure (Figure 3). The effective creation of a UV receptor was successfully demonstrated with visual signalling (LED lights) and wing flapping (actuation) (Figure 4). Our work, realized through conventional chemistry and 3D printing, offers a new paradigm for situated robotics, particularly where environmental adaptiveness and autonomous functional growth are required.

4 Methods

Vascularization. The vascular structure was designed in Autodesk Fusion, sliced in Orca Slicer, and printed either on Bambu Lab A1 with a 0.2 mm nozzle (printing configuration in Supplementary file 1) or Prusa Research Original Prusa XL Five-Head with a 0.25 mm nozzle with a built-in load cell probe (printing configuration in Supplementary file 2) out of Bambu PETG Translucent Clear. Both printers used a Smooth High Temp Plate. For explicit control, vascular structures were designed as two nested bodies: a distributed permeability infill and an encapsulation, both with a 0.1 mm layer height. The distributed permeability area consisted of 3 layers at 25% rectilinear infill. The encapsulation consisted of two bottom layers and five top layers, totalling 1 mm for the whole structure. The default (100%) bridging layer density was used. The encapsulation was leakproofed by ironing each layer at 8% ironing flow and 0.1 mm ironing line spacing. Bambu Liquid Glue was used for promoting bed adhesion. Logistic highways (veins) were designed with a rectangular cross-section of 1 mm width and 1.4 mm height, positioned above the distributed permeability area to ensure consistent liquid access. Occasional minor encapsulation defects were corrected using a UV-curable glue. A pause command was inserted after the second layer for manual electrode placement.

Receptor electrode placement procedure. The electrodes consisted of a pair of 30 μm gold wires (Surepure Chemetals LLC, USA) and placed using an in-house built wire placement device constructed by repurposing a CNC Kitchen hot melt insert installation adapter (TS100/ TS101 version) with a male M5 thread, combined with Pine64 soldering iron Pinecil V2 (Supplementary Figure S3). The base of the electrode placement device was an M5 brass hot melt insert. A custom sterling silver blade with a tip width of 1 mm was soldered to the insert. Two glass capillaries (BLAUBRAND intraMark BRAND 708733 50 μL) were melted together, drawn into a double cone, and trimmed to length. The capillaries were bonded to a silver blade using CorroProtect Exhaust Paste. The device was operated by feeding a gold wire pair through glass capillaries and guiding it by matching two indentations at the blade, ensuring approximately 130 μm spacing. Careful manual operation of the heated 195 $^{\circ}\text{C}$ blade with minimal pressing embedded the wires into the substrate polymer. This also resulted in the wires being over-molded by the molten polymer, raising them slightly above the surrounding substrate. The abrasive action of the indents kept the electrode tops exposed to the circulatory system. For the thorax section, the electrodes were terminated outside the print area for external connection. For the wing, the wires were accessed via a printed-in passthroughs and fixed with conductive paint (MGChemicals, 843WB).

Vascularization was visualised with isopropanol (Honeywell, 33539), and 1:1 vol% mixture of deionised water and isopropanol with a blue tracer (Pilc Pig Blue, Smooth-On).

UV Photopolymerisation and photolithography. Pyrrole (Py, Sigma, 102394738) was distilled under reduced pressure and stored under argon at -18°C . Cellulose acetate propionate (CAP, avg Mn \sim 15 000 by GPC, Aldrich 340642) was used to enhance mechanical properties [45]. Bis(4-methylphenyl)iodonium hexafluorophosphate (98%, 726192 Aldrich) was used as a photoinitiator, similarly to literature [31]. 15:30:1 weight ratio of Py:initiator:CAP was used. A 365-nm light-emitting diode (CUN66A1B, Seoul Viosys, Republic of Korea) source was used to photopolymerise PPy with 60 s of illumination time. Negative contact masks for directing UV-light were made with aluminium tubing, 3D-printed holders (designed in Solidworks 2020, sliced in PrusaSlicer, and printed on a Prusa i3 MK3S+ printer with PETG), and aluminium tape. The LED was driven at 1.6 W and placed at 43 mm from the sample. Molecular structures in Figure 3e were drawn using Ketcher (version 3.4.0)

Masks seen in Figure 3d were designed in Autodesk Fusion and printed on Bambu A1 with 0.2 mm nozzle and Prusa Research Original Prusa XL Five-Head with 0.25 mm nozzles. The negative masks were printed with Prusa Research Prusament PETG Jet Black at 0.2 mm single layer on a transparent substrate, with two 0.1 –mm layers of Bambu PETG Translucent Clear. Both substrate layers were ironed. Minor corrections were made to the positive mask with a carving knife and black ink.

Spectrometry. Optical density of PPy-PETG was monitored *in situ* during photopolymerization in transmission mode using Thorlabs CCS200/M spectrometer (specter collection time interval 150 ms, ThorSpectra software). In addition to the UV LED used to initiate synthesis, a separately controlled white LED was superimposed on the incident radiation to broaden the spectral range of optical density monitoring (without affecting synthesis). The integrated 580 nm peak was used as a marker of the progression of synthesis. Data processing, including smoothing and normalization, was performed using National Instruments' LabVIEW 2020.

Electrical characterization. Biologic BP-300 electrochemical impedance analyzer was used to monitor impedance in PEIS mode, constant 115 Hz, and 10 mV amplitude (Figure 3g). For Supplementary Figure S2, constant 105 Hz (Py-PETG) and constant 120 Hz (PPy-PETG) was used with 10 mV amplitude, Savitzky-Golay filter (window size 21 and polynomial order 3) was applied with Python for data processing. Oscilloscope (Rigol DS1054) was used to capture transients in Fig 3f.

Embedded receptor. An embedded impedance measurement system was designed based on the ATtiny43U microcontroller clocked at 1 MHz, programmed with an Atmel-ICE in-circuit debugger and MPLAB X IDE, and powered by an onboard 10-mAh single-cell lithium-polymer battery (4.2 V nominal). A voltage divider, formed by a linear variable resistor set to 460 k Ω and the PPy, was applied intermittent alternating-polarity constant-voltage pulse pairs (two times 200 ms) using the processor's digital input-output pins. The pulse pairs were applied at 1.4 s intervals, and the outputs were switched to high-impedance state in between pulses to minimize receptor charging effects. The average of eight consecutive ratiometric voltage readings from the 10-bit ADC channel was used to approximate impedance. The impedance readout was fed into a 3-s circular buffer. The buffer data was converted to impedance rate.

The magnitude and sign of the impedance rate were indicated using LED-based signaling. 'Signal detected' mode was enacted by four successive 4-Hz LED blinks, corresponding to the impedance rate exceeding a 2 k Ω threshold, whereas the color of the active LED - red or yellow - indicated its sign (decrease or increase, respectively). A single 0.5 s simultaneous blink of both LEDs indicated

the impedance rate was below the threshold. Count-based glitch filtering was implemented using a five-count circular buffer: five consecutive impedance-decrease readings triggered a 65 s 'reaction' mode that activated the wing-flapping mechanism (thorax receptor only), accompanied by the red LED blinking rapidly ten times.

Flapping wing mechanism. Nitinol wire (nitinolxy 0.5 mm 45 °C transition temperature) was woven in 14 passes, 13 mm each, between the thorax and the wing sections. The binary logic-level control signal from the embedded receptor was applied to the gate of an n-type MOSFET (PHB66NQ03LT) that connected the Nitinol wire to an external power source, causing Nitinol to recover the programmed straight shape using electrothermal activation. One flap consisted of 5 s activation at 6.6 W, followed by 60 s for natural convective cooling. A recoil spring and rubber bands aided the return to the starting position.

SEM imaging. Hitachi TM3000 scanning electron microscope with back-scatter electron detector and 15-kV acceleration voltage was used for Figure 1a inset and Figure 2c, d. For Figure 1a inset, the sample was cryofractured in liquid nitrogen to obtain a smooth cross-section, air-dried overnight, and then sputter-coated (Leica EM ACE600 Sputter Coater, Wetzlar) with 5 nm of gold. For Figure 2c and d, prior to imaging, samples were washed using an isopropanol:water 1:1 by volume mixture, air-dried, and subsequently cryofractured in liquid nitrogen. The fractured samples were then dried under a vacuum until the pressure reached 2-3 mPa and sputter-coated with 7 nm of gold (999).

Optical Imaging. Sony FX30 and Sony A6300 were used for optical imaging and recording at 100 and 25 FPS, respectively. Adobe Photoshop was used to remove the background in Figure 4a, d. Python code was used to extract receptor LED blinking from cropped video frames by first high-pass filtering the transient values of red or yellow hues to remove drift, and then thresholding to extract switching moments.

Biological Models. The blue underwing (*Catocala fraxini*) was chosen for its size and relative local abundance. Dead specimens were obtained from the preserved catches of the national biodiversity monitoring program, collected in summer 2023 from northeastern Estonia using a light trap. For Figure 1a left, the specimen was dried in position and pinned. To visualise the wing veins and membrane (Figure 1a right), the specimen was infused with silicone oil (5 cSt, Carl Roth) due to its high permeability through the exoskeleton and low evaporation rate. The scales were carefully removed using a paintbrush.

Large Language Models. Microsoft Copilot (GPT-5.2; Microsoft Corporation; accessed December 2025–January 2026) was employed as an assistive tool for embedded microprocessor programming and Python-based script development, including LED intensity analysis and data visualization. All AI-assisted outputs were critically reviewed, validated, and revised by the authors to ensure scientific accuracy and reproducibility.

Acknowledgements

The authors thank Prof. Toomas Tammaru and Kadri Ude (Institute of Ecology and Earth Sciences, University of Tartu) for providing *C. fraxini* specimens and scientific discussions. This research was supported by the Estonian Research Council grants PRG1498 and TEM-TA56.

Conflict of Interest

The authors declare no conflict of interest.

Author Contributions Statement

Conceptualization: K.A.P., E.S., I.M.; Data Curation: K.A.P., L.Z.; Funding Acquisition: T.T, A.A., I.M.; Investigation: K.A.P., L.Z., H.P., A.M.; Methodology: K.A.P, L.Z., H.P., U.J.; Project Administration: I.M.; Supervision: T.T., I.M.; Validation: K.A.P., L.Z., I.M.; Visualization: K.A.P., L.Z., I.M.; Writing: K.A.P, L.Z., I.M.; All authors contributed to results discussions and manuscript editing.

Data Availability Statement

All data needed to support the conclusions of this manuscript are included in the main text or Supplementary Information. Additional data could be made available from the corresponding authors K.A.P. and I.M. upon reasonable request.

References

- [1] Rolf Pfeifer, Max Lungarella, and Fumiya Iida. Self-Organization, Embodiment, and Biologically Inspired Robotics. *Science*, 318(5853):1088–1093, 11 2007.
- [2] Andrea Alù, Andres F Arrieta, Emanuela Del Dottore, Michael Dickey, Samuele Ferracin, Ryan Harne, Helmut Hauser, Qiguang He, Jonathan B Hopkins, Lance P Hyatt, Suyi Li, Stefano Mariani, Barbara Mazzolai, Alessio Mondini, Aniket Pal, Daniel J Preston, Anoop Rajappan, Jordan R Raney, Pedro M Reis, Stephen A Sarles, Metin Sitti, Uba K Ubamanyu, Martin van Hecke, and K W Wang. Roadmap on embodying mechano-intelligence and computing in functional materials and structures. *Smart Materials and Structures*, 34(6):063501, 2025.
- [3] Marie Vihmar, Daniels Bambals, Alvo Aabloo, and Indrek Must. Silk-inspired in situ web spinning for situated robots. *npj Robotics*, 3(3), 2 2025.
- [4] Daniela Rus and Michael T Tolley. Design, fabrication and control of soft robots. *Nature*, 521(7553):467–475, 2015.
- [5] Eric Sihite, Arash Kalantari, Reza Nemovi, Alireza Ramezani, and Morteza Gharib. Multi-Modal Mobility Morphobot (M4) with appendage repurposing for locomotion plasticity enhancement. *Nature Communications*, 14(1):3323, 2023.
- [6] Robert Baines, Sree Kalyan Patiballa, Joran Booth, Luis Ramirez, Thomas Sipple, Andonny Garcia, Frank Fish, and Rebecca Kramer-Bottiglio. Multi-environment robotic transitions through adaptive morphogenesis. *Nature*, 610(7931):283–289, 2022.
- [7] Max Polzin, Qinghua Guan, and Josie Hughes. Robotic locomotion through active and passive morphological adaptation in extreme outdoor environments. *Science Robotics*, 10(99):eadp6419, 2 2025.

- [8] Sachin Sachin, Alessio Mondini, Stefano Mariani, Emanuela Del Dottore, and Barbara Mazzolai. BeeRootBot: A Bioinspired Robotic Probe Exhibiting Apical Growth through In Situ Soil Binding. *Advanced Intelligent Systems*, 8(2):2500720, 9 2025.
- [9] Kevin W Lewis, Stephen Peters, Kurt Gonter, Shaunna Morrison, Nicholas Schmerr, Ashwin R Vasavada, and Travis Gabriel. A surface gravity traverse on Mars indicates low bedrock density at Gale crater. *Science*, 363(6426):535–537, 2 2019.
- [10] S Terryn, J Brancart, E Roels, G Van Assche, and B Vanderborght. Room Temperature Self-Healing in Soft Pneumatic Robotics: Autonomous Self-Healing in a Diels-Alder Polymer Network. *IEEE Robotics & Automation Magazine*, 27(4):44–55, 2020.
- [11] Hedan Bai, Young Seong Kim, and Robert F Shepherd. Autonomous self-healing optical sensors for damage intelligent soft-bodied systems. *Science Advances*, 8(49):eabq2104, 12 2022.
- [12] Elgar Kanhere, Théo Calais, Snehal Jain, Aby Raj Plamootil Mathai, Aaron Chooi, Thileepan Stalin, Vincent Sebastian Joseph, and Pablo Valdivia y Alvarado. Upgrading and extending the life cycle of soft robots with in situ free-form liquid three-dimensional printing. *Science Robotics*, 9(97):eadn4542, 12 2024.
- [13] Shibo Zou, Sergio Picella, Jelle de Vries, Vera G Kortman, Aimée Sakes, and Johannes T B Overvelde. A retrofit sensing strategy for soft fluidic robots. *Nature Communications*, 15(1):539, 2024.
- [14] R Monahan-Earley, A M Dvorak, and W C Aird. Evolutionary origins of the blood vascular system and endothelium. *Journal of Thrombosis and Haemostasis*, 11(s1):46–66, 6 2013.
- [15] Mary K Salcedo, Brian H Jun, John J Socha, Naomi E Pierce, Pavlos P Vlachos, and Stacey A Combes. Complex hemolymph circulation patterns in grasshopper wings. *Communications Biology*, 6(1):313, 2023.
- [16] Günther Pass. Beyond aerodynamics: The critical roles of the circulatory and tracheal systems in maintaining insect wing functionality. *Arthropod Structure & Development*, 47(4):391–407, 2018.
- [17] Cheng-Chia Tsai, Richard A Childers, Norman Nan Shi, Crystal Ren, Julianne N Pelaez, Gary D Bernard, Naomi E Pierce, and Nanfang Yu. Physical and behavioral adaptations to prevent overheating of the living wings of butterflies. *Nature Communications*, 11(1):551, 2020.
- [18] Artis Brasovs, Alexandre V Palaoro, Pavel Aprelev, Charles E Beard, Peter H Adler, and Konstantin G Kornev. Haemolymph viscosity in hawkmoths and its implications for hovering flight. *Proceedings of the Royal Society B: Biological Sciences*, 290(1997):20222185, 4 2023.
- [19] Stephanie Ehlers and Stefan Schulz. The scent chemistry of butterflies. *Natural Product Reports*, 40(4):794–818, 2023.
- [20] Brandon Pratt, Tanvi Deora, Thomas Mohren, and Thomas Daniel. Neural evidence supports a dual sensory-motor role for insect wings. *Proceedings of the Royal Society B: Biological Sciences*, 284(1862):20170969, 9 2017.
- [21] Jose M Ayuso, María Virumbrales-Muñoz, Joshua M Lang, and David J Beebe. A role for microfluidic systems in precision medicine. *Nature Communications*, 13(1):3086, 2022.

- [22] Nikola A Dudukovic, Erika J Fong, Hawi B Gameda, Joshua R DeOtte, Maira R Cerón, Bryan D Moran, Jonathan T Davis, Sarah E Baker, and Eric B Duoss. Cellular fluidics. *Nature*, 595(7865):58–65, 2021.
- [23] Xiaojiang Liu, Ming Gao, Boyuan Li, Ruoyu Liu, Zhejun Chong, Zhongze Gu, and Kun Zhou. Bioinspired Capillary Transistors. *Advanced Materials*, 36(41):2310797, 10 2024.
- [24] Cameron A Aubin, Snehashis Choudhury, Rhiannon Jerch, Lynden A Archer, James H Pikul, and Robert F Shepherd. Electrolytic vascular systems for energy-dense robots. *Nature*, 571(7763):51–57, 2019.
- [25] M Garrad, G Soter, A T Conn, H Hauser, and J Rossiter. A soft matter computer for soft robots. *Science Robotics*, 4(33), 2019.
- [26] Kadri-Ann Valdur, Tarmo Tamm, Isabella Fiorello, Alvo Aabloo, Indrek Must, Edoardo Sinibaldi, and Barbara Mazzolai. A Spider Leg-Inspired mm-Scale Soft Exoskeleton Enabled by Liquid via Hydration and Charge Transport. *Advanced Functional Materials*, 34(28):2315161, 7 2024.
- [27] Jeroen Rouwkema, Nicolas C Rivron, and Clemens A van Blitterswijk. Vascularization in tissue engineering. *Trends in Biotechnology*, 26(8):434–441, 2008.
- [28] Miriam Filippi, Thomas Buchner, Oncay Yasa, Stefan Weirich, and Robert K Katzschmann. Microfluidic Tissue Engineering and Bio-Actuation. *Advanced Materials*, 34(23):2108427, 6 2022.
- [29] Robert Baines, Frank Fish, Josh Bongard, and Rebecca Kramer-Bottiglio. Robots that evolve on demand. *Nature Reviews Materials*, 9(11):822–835, 2024.
- [30] Kiarash Arangdad, Erol Yildirim, Andrew Detwiler, Curtis D Cleven, Christopher Burk, Renzo Shamey, Melissa A Pasquinelli, Harold S Freeman, and Ahmed El-Shafei. Influence of UV stabilizers on the weathering of PETG and PCTT films. *Journal of Applied Polymer Science*, 136(47):48198, 12 2019.
- [31] J F Rabek, J Lucki, M Zuber, B J Qu, and W F Shi. Polymerization of pyrrole by cationic photoinitiators. *Polymer*, 33(22):4838–4844, 1992.
- [32] Neha Luhakhra and Sanjiv Kumar Tiwari. Polaron and bipolaron mediated photocatalytic activity of polypyrrole nanoparticles under visible light. *Colloids and Surfaces A: Physicochemical and Engineering Aspects*, 667:131380, 2023.
- [33] Yuke Yan, Xinyue Liu, Chuanjie Liu, Zhou Li, Huiru Yun, Yanfei Zhao, and Fei Zhao. Tailoring Topological Network of Conductive Hydrogel for Electrochemically Mediated Encryption. *Advanced Materials*, 38(4):e07637, 10 2025.
- [34] Pavel Galář, Branislav Dzurňák, Petr Malý, Jan Čermák, Alexander Kromka, Mária Omastová, and Bohuslav Rezek. Chemical Changes and Photoluminescence Properties of UV Modified Polypyrrole. *International Journal of Electrochemical Science*, 8(1):57–70, 2013.
- [35] Jean Luc Bredas and G Bryan Street. Polarons, bipolarons, and solitons in conducting polymers. *Accounts of Chemical Research*, 18(10):309–315, 10 1985.
- [36] Yukio-Pegio Gunji, Andrew Adamatzky, Panagiotis Mougkogiannis, and Andrei Khrennikov. Quantum-like coherence derived from the interaction between chemical reaction and its environment. *Discover Artificial Intelligence*, 6(1):96, 2026.

- [37] Yikai Zheng, Subir Ghosh, and Saptarshi Das. A Butterfly-Inspired Multisensory Neuromorphic Platform for Integration of Visual and Chemical Cues. *Advanced Materials*, 36(13):2307380, 3 2024.
- [38] Chaoqun Dong, Alejandro Carnicer-Lombarte, Filippo Bonafè, Botian Huang, Sagnik Middy, Amy Jin, Xudong Tao, Sanggil Han, Manohar Bance, Damiano G Barone, Beatrice Fraboni, and George G Malliaras. Electrochemically actuated microelectrodes for minimally invasive peripheral nerve interfaces. *Nature Materials*, 23(7):969–976, 2024.
- [39] Yuedan Wang, Zhou Zhou, Xing Qing, Weibing Zhong, Qiongzhen Liu, Wenwen Wang, Mufang Li, Ke Liu, and Dong Wang. Ion sensors based on novel fiber organic electrochemical transistors for lead ion detection. *Analytical and Bioanalytical Chemistry*, 408(21):5779–5787, 2016.
- [40] Ge Cao, Anqi Wu, Chuhan Zhang, ShiJia Zhang, Zhenyu Wang, and Enhou Han. Highly dispersed polypyrrole nanotubes enhance the corrosion resistance of polyurethane coatings. *Colloids and Surfaces A: Physicochemical and Engineering Aspects*, 725:137697, 2025.
- [41] Akif Kaynak, Joe Unsworth, Ray Clout, Ananda S Mohan, and Geoffrey E Beard. A study of microwave transmission, reflection, absorption, and shielding effectiveness of conducting polypyrrole films. *Journal of Applied Polymer Science*, 54(3):269–278, 10 1994.
- [42] Congqi Qi, Bohan Liu, Zheqi Chen, and Yingwu Luo. Multimaterials by Patterning Microphase Separation of a Single Copolymer. *Advanced Materials*, 38(9):e17801, 12 2025.
- [43] Artem I Leonov, Alexander J S Hammer, Slawomir Lach, S Hessam M Mehr, Dario Caramelli, Davide Angelone, Aamir Khan, Steven O’Sullivan, Matthew Craven, Liam Wilbraham, and Leroy Cronin. An integrated self-optimizing programmable chemical synthesis and reaction engine. *Nature Communications*, 15(1):1240, 2024.
- [44] Chenru Duan, Guan-Horng Liu, Yuanqi Du, Tianrong Chen, Qiyuan Zhao, Haojun Jia, Carla P Gomes, Evangelos A Theodorou, and Heather J Kulik. Optimal transport for generating transition states in chemical reactions. *Nature Machine Intelligence*, 7(4):615–626, 2025.
- [45] Zhuqun Shi, Huichang Gao, Jiao Feng, Beibei Ding, Xiaodong Cao, Shigenori Kuga, Yingjun Wang, Lina Zhang, and Jie Cai. In Situ Synthesis of Robust Conductive Cellulose/Polypyrrole Composite Aerogels and Their Potential Application in Nerve Regeneration. *Angewandte Chemie International Edition*, 53(21):5380–5384, 5 2014.